Corrosion Science 210 (2023) 110828

Contents lists available at ScienceDirect

Corrosion Science

journal homepage: www.elsevier.com/locate/corsci

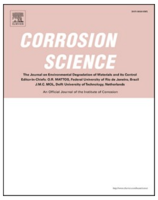

Passivity of AlCrFeMnTi and AlCrFeCoNi high–entropy alloys in Hanks' solution

Ayoub Tanji [a], Rui Feng [b], Zongyang Lyu [b], Ridwan Sakidja [c], Peter K. Liaw [b], Hendra Hermawan [a,*]

[a] Department of Mining, Metallurgical and Materials Engineering, Laval University, Quebec City, QC G1V 0A6, Canada
[b] Department of Materials Science and Engineering, The University of Tennessee, Knoxville, TN 37996, USA
[c] Department of Physics Astronomy and Materials Science, Missouri State University, Springfield, MO 65897, USA

ARTICLE INFO

Keywords:
Alloy
AFM
EIS
Polarization
Modeling studies
Passivity
Passive films

ABSTRACT

The present work studies the passivation characteristic and corrosion resistance of $Al_{20}Cr_5Fe_{50}Mn_{20}Ti_5$ and $Al_7Cr_{23.26}Fe_{23.26}Co_{23.26}Ni_{23.26}$ high–entropy alloys in Hanks' solution at 37 °C, in view of potential biomedical applications. The $Al_7Cr_{23.26}Fe_{23.26}Co_{23.26}Ni_{23.26}$ possesses a higher corrosion resistance than Ti-6Al-4 V alloy, mainly due to the formation of a stable p–type passive film composed of $Cr(OH)_3$, Cr_2O_3, CoO, Co_3O_4, and $Ni(OH)_2$, leading to low vacancy concentration and limited ion conductivity. The $Al_{20}Cr_5Fe_{50}Mn_{20}Ti_5$ exhibits an n–type passive film composed of Fe_2O_3, $Fe(OH)_3$, TiO_2, and MnO_2 that promotes chloride ions adsorption and diffusion–controlled corrosion, while its microstructural precipitates allowed a selective dissolution.

1. Introduction

High corrosion–resistant alloys have been used as materials for biomedical implants (biomaterials) since the invention of stainless steel in 1920 s and are still in use today. Each year, millions of implants are commercially made of 18Cr-14Ni-2.5Mo stainless steel (ASTM F138), Ti-6Al-4 V (ASTM F136), Co-28Cr-6Mo (ASTM F75), 50Ni-50Ti (ASTM F2063) [1]. The biocompatibility of these alloys is ensured through their high corrosion resistant, which comes from the formation of passive film (mainly composed of Cr and Ti oxides) that prevent the release of their high content of allergenic, toxic/cytotoxic or carcinogenic elements (e.g., Ni, Co, Cr, V, Al) to the body [2,3]. The fundamental paradigm of metallic biomaterials has been "the more corrosion resistant, the more biocompatible" [4,5]. With a high corrosion resistance in vitro (in chloride-containing simulated body fluids), a high corrosion resistance (inertness) in vivo could be anticipated. Therefore, biomaterials are often required to be tested for corrosion before they are approved by regulatory organizations. Many new materials have been proposed as potential biomaterials, including several high–entropy alloys (HEAs) [6–8]. HEAs are alloys of several principal elements with equal or near equal–molar fractions that form simple solid–solution phases instead of complex multi–phase microstructures consisting of intermetallics [9–11]. The HEAs microstructures provide unique properties when compared to conventional alloys, such as high strength and oxidation resistance, attractive to many applications [12–14]. Many HEAs demonstrated a high corrosion resistance resulting from their unique chemical composition and their solid–solution microstructure [15,16]. A homogenous microstructure, high strength and ductility, and high corrosion resistance are the key features of potential biomaterials for biomedical implants.

In comparison with conventional alloys, studies have reported high wear resistance, wettability, and pitting corrosion resistance for TiZrTaHfNb [17], and high strength for TiZrHfCrMo and TiZrHfCoCrMo [18], as well as high cellular adhesion for TiNbTaZrMo [19]. The $(MoTa)_xNbTiZr$ medium– and high–entropy alloys exhibited a combination of strong passive behavior and non–toxic soft tissue response with high mechanical properties [20]. Other works focused on the study of microstructure and electronic structure and their effects on the mechanical properties required for biomedical application to select potential HEAs. Among them is the design–approach study to predict HEAs properties based on the use of quantum mechanical metrics on 13 biocompatible HEAs and modeling of the porosity to reduce the Young's modulus to the values close to that of bone [21]. Another work investigated the single–crystal elastic properties of 21 Ti–containing HEAs to

---

* Correspondence to: Department of Mining, Metallurgical and Materials Engineering Pavillon Adrien-Pouliot, local 1722-B Université Laval 1065 avenue de la Medecine Québec, Québec, G1V 0A6, Canada.

E-mail address: hendra.hermawan@gmn.ulaval.ca (H. Hermawan).

https://doi.org/10.1016/j.corsci.2022.110828
Received 24 August 2022; Received in revised form 14 October 2022; Accepted 12 November 2022
Available online 18 November 2022

study the effect of harnessing elastic anisotropy on elastic properties, and concluded that the valence electron count has a dominant influence on Young's modulus and torsion modulus in the HEAs [22].

The family of AlCrFe–*XY* HEAs, of which *X* and *Y* are other chemical elements, have been widely studied for their expected high corrosion resistance due to the presence of passivating elements mainly Cr [23–25]. Chromium facilitates the formation and growth of a passive protective barrier/film on the surface in NaCl solution [26,27]. In AlCrFeCoNi, an increase in Al from 6.96 to 14.80 at% leads to a deterioration of the film resistance to pitting due to film thickening and increasing volume fractions of the (Al, Ni)–rich and Cr–depleted BCC phase [28]. A galvanic coupling formed between the FCC–enriched Fe–Cr precipitates and the Al–Ni–enriched B2 matrix was found to govern the corrosion mechanism of AlCrFeCoNi in a 0.6 M NaCl solution at room temperature [29], which was also found for the equi–atomic AlCrFeCoNi fabricated by selective electron beam melting [30]. This alloy, when applied as coatings by high–velocity–oxygen–fuel spraying, well protects sintered NdFeB magnets against corrosion because of the increasing charge transfer resistance and the reducing corrosion current density [31]. In another case, a plasma–sprayed AlCrFeCoNi coating showed polarization behavior identical to that of SS316L, presenting prospects as corrosion resistant materials [32]. Differently, AlCrFeMnTi has been proposed as a lightweight HEAs for high-temperature applications for its energy efficiency [33]. The alloy is characterized by the presence of the BCC, C14–Laves and $L2_1$ phases, where $L2_1$ is homogeneously distributed in the BCC phase [33], but the corrosion aspect of the alloy is less known in the literature.

Many clinical reports reveal that cases of implant corrosion are not uncommon on current medical grade corrosion resistant alloys, partly due to the limitation of standard test methods for detecting corrosion at the microscopic level and revealing its mechanism [34,35]. The present work aims at revealing the underlying mechanism that governs the passivation and corrosion processes of $Al_{20}Cr_5Fe_{50}Mn_{20}Ti_5$ and $Al_7Cr_{23.26}Fe_{23.26}Co_{23.26}Ni_{23.26}$ HEAs in a Hanks' solution at 37 °C, based on combined analyses of data obtained from electrochemical tests [cyclic potentiodynamic polarization (CPP), electrochemical impedance spectroscopy (EIS), and potentiostatic polarization test (PPS)] and surface characterizations [scanning electron microscopy (SEM), atomic force microscopy (AFM), and X–ray photoelectron spectroscopy (XPS)]. By revealing microstructure–dependent passive–film characteristics through complementary modeling studies (high–electrical–field, anodic–dissolution and film–growth as well as the point–defect models), which demonstrate the controlling process during passivation and localized corrosion, the present work will advance the fundamental understanding of localized corrosion mechanism that will be useful for future alloy design and for ensuring that corrosion will not be an issue once the alloys are made into biomedical implants. This work is an electrochemical biocompatibility evaluation, no data on cytotoxicity or biological biocompatibility were provided as they will be the subject of future works.

2. Experimental

2.1. HEAs preparation

Two samples of HEAs: $Al_{20}Cr_5Fe_{50}Mn_{20}Ti_5$ (HEA1), and $Al_7Cr_{23.26}Fe_{23.26}Co_{23.26}Ni_{23.26}$ (HEA2) were prepared from alloying elements of 99.9 (wt%) purity. The HEA1 was fabricated using an arc melting method where the ingot was melted at least six times before drop–casting to ensure chemical homogeneity. The HEA2 was fabricated by a vacuum induction melting followed by a hot isostatic pressing at 103 MPa, 1204 °C for 4 h, and a 2 h homogenization at 1200 °C before water quench. A granular microstructure was observed for both HEA samples, with an average grain size of 30 μm and 500 μm for HEA1 and HEA2, respectively. A formation of high density coherent $L2_1$ precipitates in a disordered BCC solid solution matrix was detected in HEA1, while a single FCC phase was detected in HEA2. In general, the $L2_1$ precipitates contain more concentrations of Al and Fe than the BCC or C14 phases within the AlCrFeMnTi HEAs, as reported in the previous works [33,36,37]. As the two HEAs have different chemical composition and processing history, different electrochemical behavior was expected and not to be directly compared to each other. A comparison was made to Ti-6Al-4 V alloy representing a standard metallic biomaterial.

2.2. Electrochemical corrosion test

The electrochemical corrosion tests were performed, using a potentiostat (CH Instruments model 760E, Austin, TX, USA) in a three–electrode cell configuration with the HEA specimen, saturated calomel electrode (SCE), and graphite rod as working, reference, and counter electrodes, respectively. Before the electrochemical tests, HEA specimens were polished with SiC papers to 2400 grit, and final polishing with 1 μm diamond suspension, and further polished with 0.05 μm colloidal silica suspensions. All tests were performed in Hanks' solution (Gibco HBSS (1X) Ref #14175–095, Fisher Scientific, Canada) maintained at 37 ± 1 °C with a measured pH of 7.2. Two electrochemical test methods were used: cyclic potentiodynamic polarization (CPP), and electrochemical impedance spectroscopy (EIS), which were started after 6 h stabilization time on the open circuit potential (E_{oc}). The CPP experiments were conducted with a scan rate of 1 mV/s from – 0.6–0.3 V vs. SCE, while the AC mode EIS experiments were done at a frequency range from 10^5 Hz to 10^{-2} Hz with an amplitude of 10 mV from the E_{oc} and an acquisition rate of 12 points per frequency decade. All the experiments were triplicated, and data were collected and analyzed, using the CH Instruments and EC–Lab software. For comparison, the electrochemical properties of the Ti-6Al-4 V alloy were also examined under the same conditions.

2.3. Metal dissolution and passive film evaluation

The alloys' dissolution rate was examined qualitatively from the surface topography, using an atomic force microscope (AFM, Oxford Instruments MFP–3D Origin+, Santa Barbara, CA, USA) with a scan size of 120 μm^2, employing a silicon probe (AC160TS–R3) in a tapping mode in air, after a potentiostatic polarization test (PSP) for 1 h under the E_{corr}. Surface observation was made on the specimens after a potentiodynamic polarization test for any sign of pitting, using a scanning electron microscope (SEM, Quanta 250 FEI, Hillsboro, OR, USA). The semiconductor characteristics of oxide films were investigated, employing the Mott–Schottky analysis in a passive–potential plateau range of – 0.35 to – 0.10 V for HEA1 and – 0.15–0.10 V for HEA2 at a fixed frequency of 1 kHz, in the cathodic direction with an increment of 0.05 V. The passivation behavior and oxides–film compositions were characterized, using an X-ray photoelectron spectroscope (XPS, PHI 5600–ci spectrometer, Physical Electronics, Chanhassen, MN, USA) in high–resolution and angle–resolved modes (AR–XPS) with an analyzed area of 0.5 mm^2 and depth of analysis from ≈ 2–10 nm. The spectra were acquired, utilizing a standard aluminum X − ray source ($K_\alpha = 1486.6$ eV) with charge compensation, while high–resolution spectra were recorded, using a standard magnesium ($K_\alpha = 1253.6$ eV).

3. Results

3.1. Electrochemical corrosion characterization

All specimens exhibited a passive behavior and tended to form a passive film on the surface (Fig. 1a, b) with the two HEAs showed higher E_{oc} values than that of Ti-6Al-4 V (Table 1). The HEA2 exhibited a stable passivation domain with a low value of i_{pass} and higher values of E_{corr} and pitting potential (E_{pit}) than HEA1 and Ti-6Al-4 V. Interestingly, HEA1 exhibited an unstable passivation plateau with multiple perturbations. A negative–type hysteresis loop was observed for HEA2, indicating the

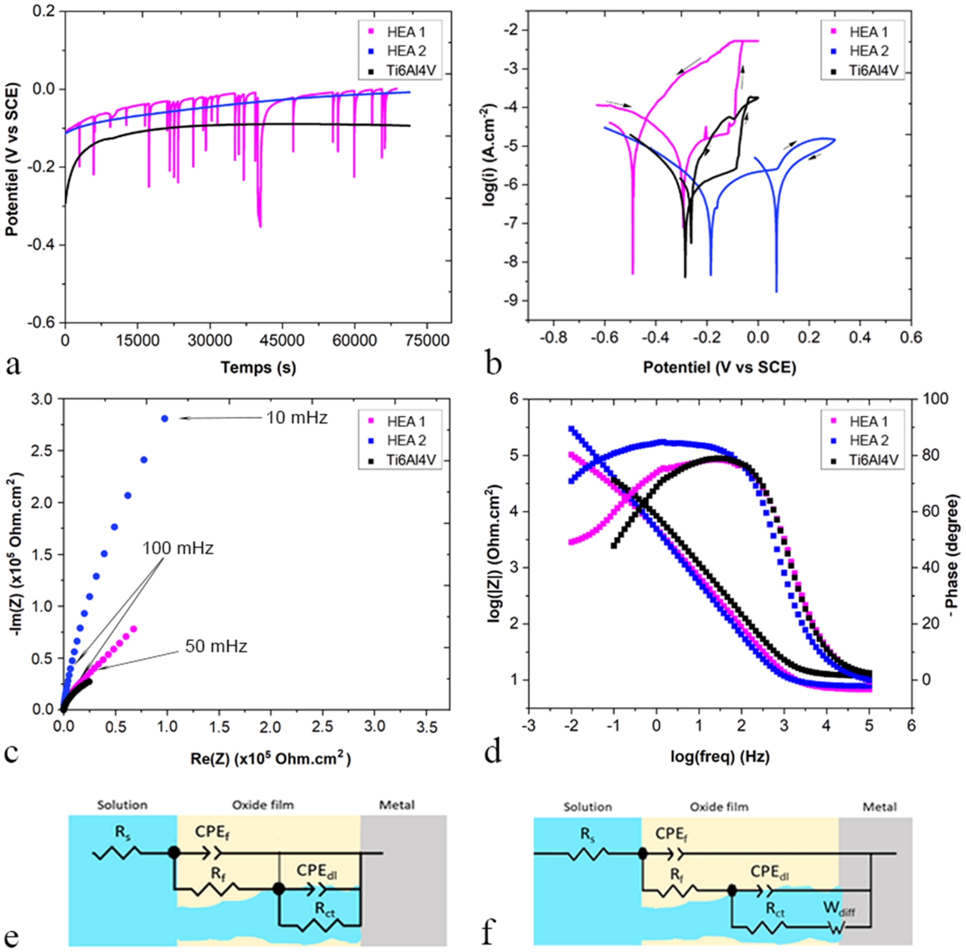

Fig. 1. Electrochemical corrosion tests results: (a) OCP curves, (b) CPP curves, (c) EIS Nyquist plots, (d) EIS Bode plots, and (e, f) proposed equivalent circuit models.

Table 1
Corrosion parameters obtained by analyzing the OCP, and CPP curves.

Specimen	E_{oc} (mV/ SCE)	E_{corr} (mV/ SCE)	i_{corr} (μA/ cm^2)	E_{pit} (mV/ SCE)	i_{pass} (μA/ cm^2)
HEA1	− 63 ± 51	− 370 ± 80	4.55 ± 3.06	− 116 ± 04	1.27 ± 0.33
HEA2	− 1 ± 12	− 153 ± 17	0.89 ± 0.38	67 ± 08	0.57 ± 0.25
Ti-6Al-4 V	− 126 ± 04	− 270 ± 11	0.52 ± 0.1	− 73 ± 04	0.87 ± 0.25

reduction of the current density during the reverse scan, while HEA1 exhibited a positive–type hysteresis loop with a potential of anodic to cathodic transition lower than E_{corr}.

The HEAs specimens exhibited a large relaxation time constant, compared to Ti-6Al-4 V, with a non–ideal semicircle observed for HEA2 and a linear variation in the Nyquist plot and a deviation in impedance and phase curves in the Bode plot at frequencies lower than 50 mHz for HEA1, as presented in Fig. 1c and d. The different behaviors in the EIS plots were modeled by the equivalent circuits shown in Fig. 1e for HEA2 and Ti-6Al-4 V, which includes resistors for the solution, oxide film, and charge transfer (R_s, R_f, and R_{ct}, respectively), constant–phase elements to account for the oxide film (CPE_f) and for the double layer (CPE_{dl}), as well as in Fig. 1f for the HEA1 containing a Warburg diffusion element. The maximum value of the phase angle was below than – 90 degrees. This behavior indicates a deviation from the ideal behavior of capacitors. For this reason, a *CPE* was used to compensate the frequency dispersion resulting from surface roughness/porosity, geometric irregularities, or variation in resistivity through the thickness [38–41]. The HEA2 has higher resistances for the film and for the charge transfer than those of HEA1 and of Ti-6Al-4 V according to the fitting results presented in Table 2. The impedances of Warburg element and *CPE* are calculated by using the following formulae:

$$Z_w = \frac{\sigma}{\sqrt{\omega}} + \frac{\sigma}{j\sqrt{\omega}} \tag{1}$$

$$Z_{CPE} = \left[Q(j\omega)^n\right]^{-1} \tag{2}$$

where Z_W is the Warburg element impedance, and σ is the Warburg coefficient of a unit $\Omega.s^{-0.5}$, and Q is the magnitude that represents a pre–factor of *CPE*, and n is the exponent of *CPE* ($-1 \le n \le 1$). The following Brug's formula [42] was used to calculate the effective capacitance:

$$C_{eff} = Q^{\frac{1}{n}} \times \left(R_s^{-1} + R^{-1}\right)^{\frac{n-1}{n}} \tag{3}$$

The dissolution rate was evaluated by the potentiostatic polarization test with an applied potential of $E = E_{corr}$. As shown in Fig. 2a, a rapid drop in the current density occurred during the first tens of seconds, followed by stabilization at very low current density values. The HEA2 has a lower steady–state plateau and starting–pick of the current density than those measured for the HEA1. The dissolution rate was qualitatively evaluated, using the surface topography measurements after the PSP test (Fig. 2c, and d). The topographical parameters were extracted from the roughness profiles on the two surfaces (Fig. 2b). The surface roughness measurement, presented in Table 3, revealed that HEA2 has the lowest values of the square mean height (S_q), arithmetic mean height

Table 2
Fitting parameters derived from the proposed equivalent circuit model.

Specimen	R_s (Ω. cm^2)	Q_f (×10^{-6} F.cm^{-2}.s$^{(n-1)}$)	C_{f_eff} (×10^{-2} F. cm^{-4})	n_f	R_f (×10^3 Ω. cm^2)	Q_{dl} (×10^{-6}F.cm^{-2}. s$^{(n-1)}$)	n_{dl}	R_{ct} (×10^6 Ω. cm^2)	C_{dl_eff} (×10^{-9} F. cm^{-2})	σ_w (×10^6 Ω. s$^{-0,5}$)
HEA1	36	6.61	2.36	0.89	0.06	1.39	0.46	0.25	0.012	0.14
HEA2	10	29.33	15.8	0.93	714.93	6.64	0.69	2.75	88	–
Ti-6Al-4V	11	19.05	11	0.91	0.20	19.09	0.58	0.13	41	–

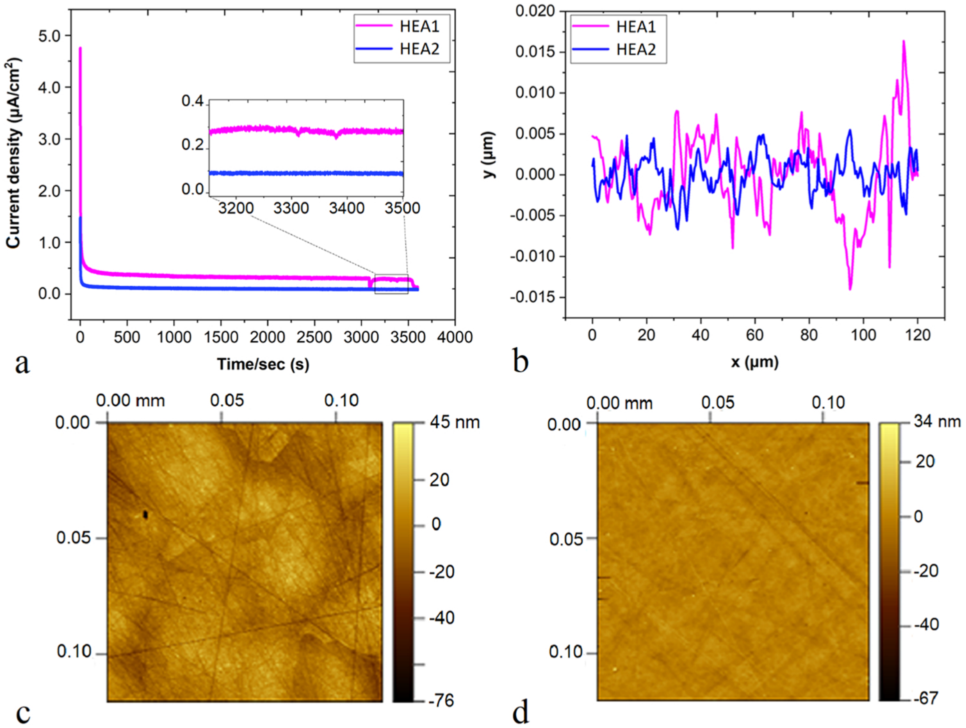

Fig. 2. Dissolution test results: (a) PSP curves, (b) topography profiles, (c, d) AFM surface topography after PSP, scan area = 120 µm for HEA1 and HEA2, respectively.

Table 3
Topographical parameters obtained from the AFM analysis.

Specimen	S_a (nm)	S_q (nm)	S_v (nm)
HEA1	8.85	10.93	50.38
HEA2	3.17	4.21	40.92

(S_a), and maximum pit height (S_v), compared to those of HEA1.

3.2. *Surface and passive film characterization*

A trace of more degradation of the passive film, in the form of deep and large pits up to 50 µm, was observed on the surface of HEA1, contrary to that of HEA2, which stayed smooth and clean after being subjected to the polarization test (Fig. 3). The surface of HEA1 experienced a strong electrochemical activity, damaging the passive film, forming pits and enlarging the existing pores. The latter is related to the formation of metal-chlorides and their hydrolysis to H^+ and Cl^- ions which decreased the pH inside the pores (local acidity) and thus accelerated the local dissolution of the metal (i.e. enlarging pores) as the result of an autocatalytic mechanism.

The passive film formed on the HEAs specimens contains a mixture of oxides, of which Al_2O_3, Cr_2O_3, $Cr(OH)_3$, FeOOH, and Fe_2O_3 were present in both, while $Al(OH)_3$ was present only in HEA1 (Fig. 4). The $Cr(OH)_3$ fraction was more important in HEA2, while HEA1 was rich in Al_2O_3, Cr_2O_3, and Fe_2O_3. Moreover, the HEA1 passive film contained oxides of TiO_2, MnO, and MnO_2, while $Ni(OH)_2$, Co_3O_4, and CoO were present in the HEA2 passive film. The O1s oxygen spectrum of the two specimens provides information on the coexistence of the Metal–O and Metal–OH bonds in the two HEAs specimens. The AR-XPS spectra indicated a major dominance of the Metal–OH bond on the outer side of the HEA2 film (Fig. 5) with Cr and Fe as the most present elements on HEA2, while the passive film of HEA1 was rich in Al and Fe.

Based on the Mott–Schottky theory, the semiconductor properties of passive films formed on the surface of HEAs can be studied by applying the following two equations [43]:

$$\frac{1}{C_s^2} = \frac{2}{\varepsilon \quad \varepsilon_0 \quad e \quad N_D}\left(E - E_{FB} - \frac{kT}{e}\right) for \quad n - type \tag{4}$$

$$\frac{1}{C_s^2} = -\frac{2}{\varepsilon \quad \varepsilon_0 \quad e \quad N_A}\left(E - E_{FB} - \frac{kT}{e}\right) for \quad p - type \tag{5}$$

where N_D and N_A are, respectively, the donor and acceptor densities in the passive film that are calculated from linear regions of the Mott-Schottky plots, e is the electron charge (1.6 × 10^{-19} C), E is the applied potential, E_{FB} is the flat band potential, T is the temperature, K is the Boltzman constant (1.38 × 10^{-23} J/K), ε is the dielectric constant, and ε_0 is the vacuum permittivity (8.8542 × 10^{-12} F.m^{-1}). The dielectric constant for a high entropy alloy is unknown, however, we estimated the dielectric constant of passive film formed of a high fraction of

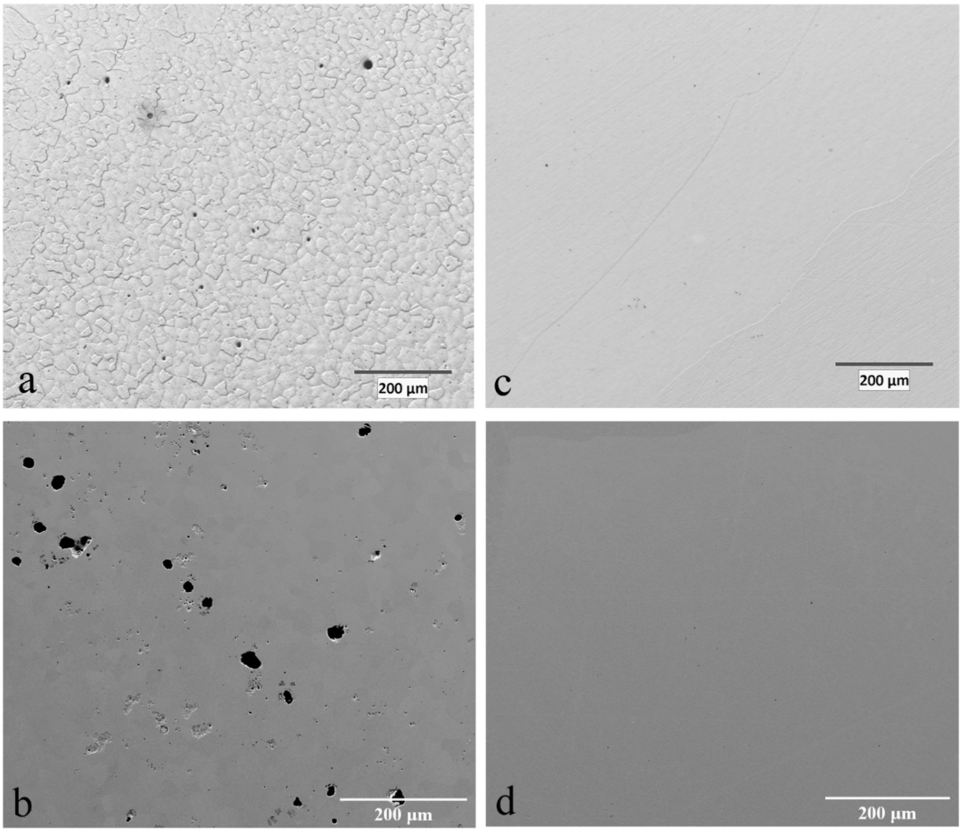

Fig. 3. (a, c) Optical micrographs after polishing and (b, d) secondary electron mode of SEM micrographs after being subjected to the polarization test (just after reaching E_{pit}): (a, b) HEA1, (c, d) HEA2.

Al– and Fe–oxides, as HEA1, as $\varepsilon = 12$, and for the case of HEA2 that is rich of Fe– and Cr–oxides, the value of $\varepsilon = 25$. These values are based on those found in the literature for the various metal oxides [44–46].

The plots presented in Fig. 6a and b display two different n– and p–type semiconductor behaviors between the two HEAs specimens. The HEA2 showed a p–type character, while HEA1 had an n–type character. The donors and acceptors densities were calculated and presented in Table 4, whose N_D of HEA1 was much higher than the N_A of HEA2.

3.3. Modeling of the passivation–process kinetics

The kinetics of the passivation process were evaluated from potentiostatic polarization tests by applying a passive potential of $E = E_{pass}$ of 0.05 V/SCE and – 0.15 V/SCE for HEA2 and HEA1, respectively. These passive polarization tests were done directly just after the active polarization tests (dissolution test) to remove the naturally formed oxide film on the surface, and to study the different passivation mechanisms on a bare surface. As shown in Fig. 6c, an identical behavior between the two specimens manifested by a rapid drop in the current density and followed by stabilization. The starting peak current density and the steady–state plateau were lower for HEA2 than those of HEA1, but the transition between the two stages was faster for HEA2 than for HEA1.

By measuring the current densities generated during the passivation process at the metal surface and based on current transient analysis theories for the high field model and for the anodic dissolution and film growth model, we can study and follow the kinetics of the processes existing simultaneously during the early time. The first model is the high–field model that relates the current density to the time and charge density according to the following equations [47–50]:

$$i = At^{-n} \tag{6}$$

$$\log i \quad (t) = \log A_1 - n\log(t) \tag{7}$$

$$\log i(t) = \log A_2 + \frac{cBV}{q(t)} \tag{8}$$

where *i(t)* is the current density, *t* is the time, *q(t)* is the charge density, A_1 is a constant, and *n* is the passivation index that can express, indirectly, the passive film growth rate, *c* is a constant related to the film, A_2 and *B* are parameters associated with the energy of activation for charges displacement, and *V* is the potential drop across the passive film. The slope (*n*) of the plot *log i(t)* vs. *log (t)* as well as (*cBV*) of the plot of *log i(t) vs. 1/q(t)* represent the passivation rate [51]. The *cBV* can also be a measure of stress corrosion cracking (SCC) susceptibility [51–53]. Two growth regimes of the passive film can be differentiated from the *log (i) vs 1/q(t)* curves: the first is at intermediate current and charge densities characterized by a low resistance to ion conduction, and the second is at low values of *i(t)* and higher values of *q(t)* characterized by a more resistant film. However, these two films are not separated, and the change in the regime produces a change in the behavior of the entire film [48].

According to the high–field model, the film–growth process is a result of ionic conduction and species migration through the film under a high electric field. This model assumes that at a very early time, the current generated during the passivation process is the result of passive mechanisms of film formation and growth without any contribution from other mechanisms. The anodic dissolution and the film–growth model demonstrated that the linear relationship between *log i(t)* and *log (t)* at early passivation times is no longer effective or valid and deviates from the – 1 slope (ideal linearity) due to the voltage drop (IR) [50,54]. Thus, the second model assumes that the anodic dissolution mechanism also contributes to the passivation current density. Then, the total current density can be expressed as [55]:

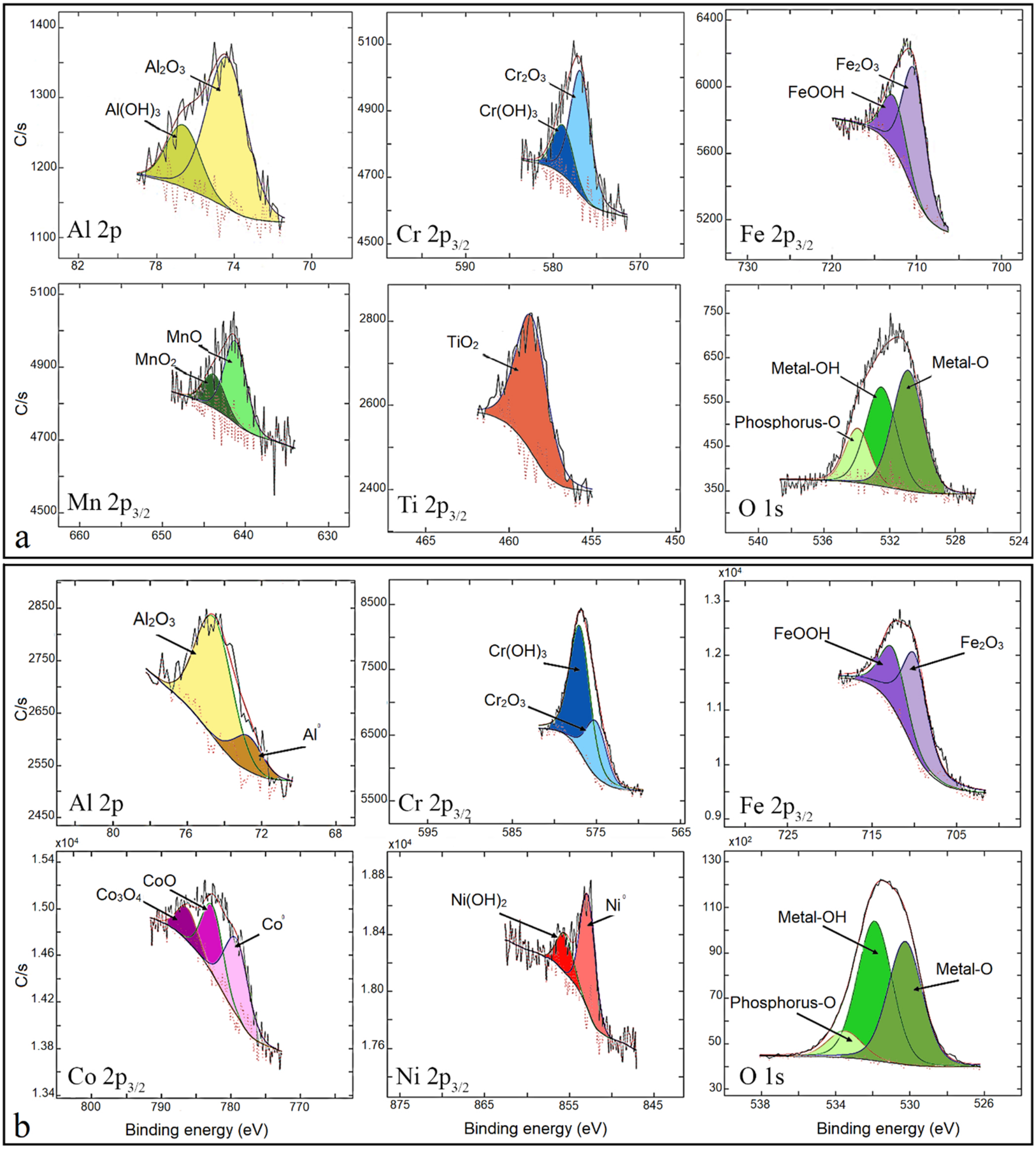

Fig. 4. XPS spectra after being subjected to a potentiodynamic polarization test for HEA1 and HEA2, respectively.

$$i_{tot} = i_{diss} + i_{film} = (1-\theta)i_{peak} + \theta A t^{-b} \tag{9}$$

where i_{peak} is the peak current density, A is a characteristic charge density coefficient, and b is a constant, and θ is the fraction of the oxide film coverage on the surface, as described by Avrami kinetics [56]:

$$\theta = 1 - \exp(-kt^n) \tag{10}$$

where k is the film growth rate, and n is the exponent associated with the reaction order of the growth mechanism (1D, 2D, or 3D dimension) and the geometry of the oxide (spheres, rods, etc.).

As shown in Fig. 6e and f, both HEAs specimens exhibited current decay curves, but the results deviated from the high–field model at an earlier stage ($t < 400$ ms) and later stage ($t > 10$ s) for the plot of *log (i) vs. log(t)* for both specimens, and the same for the plot of *log (i) vs. 1/q(t)* at ($t < 1.7$ s) and ($t < 0.75$ s) for HEA1 and HEA2, respectively. The passivation rate can be measured by the linear slope of the two plots of *log (i) vs log(t)* and *log (i) vs 1/q(t)*, of which HEA2 had a higher passivation index, *n*, and lower *cBV* value than those of HEA1 (Table 4).

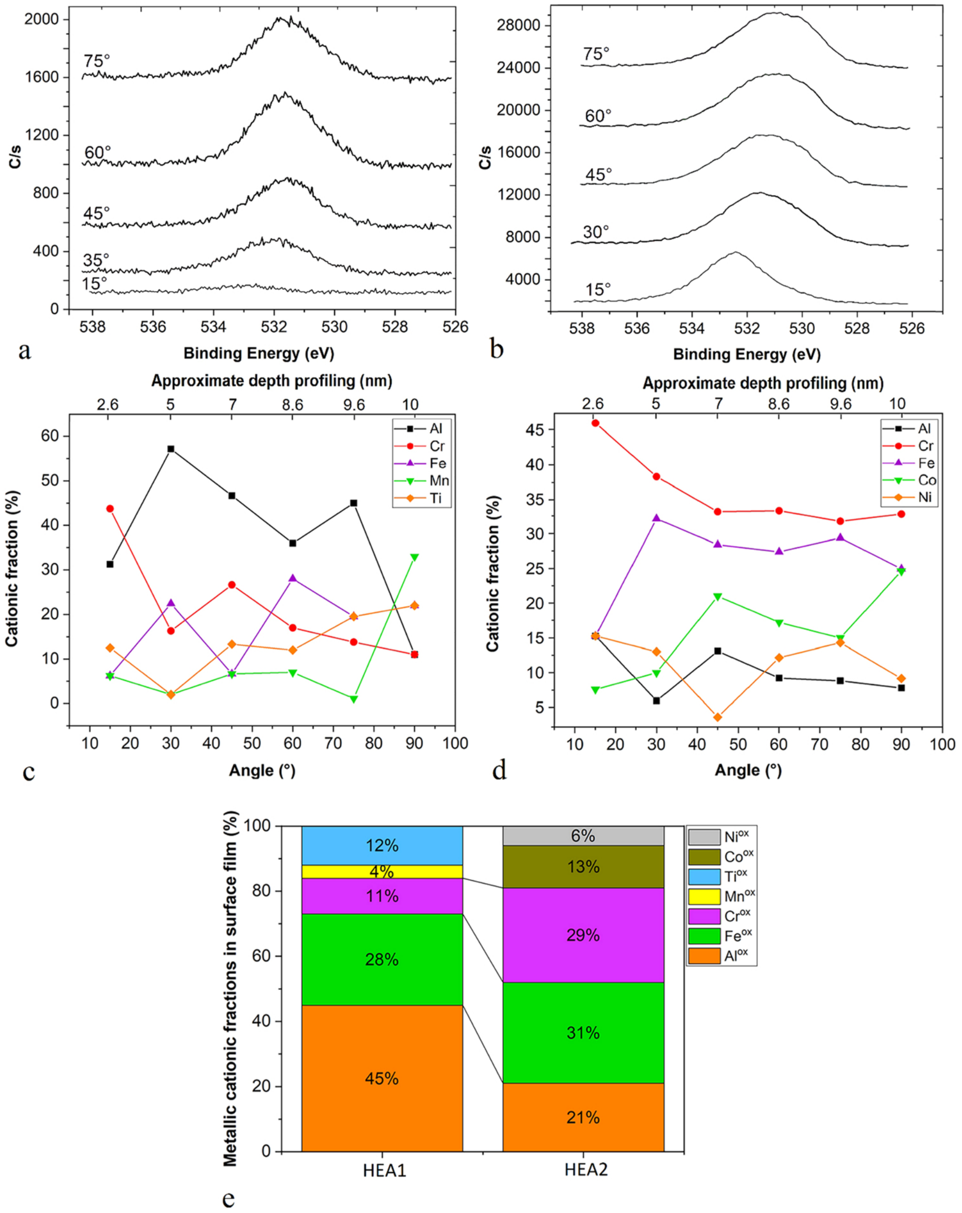

Fig. 5. AR–XPS spectra and the approximate depth profiling: (a, c) HEA1, (b, d) HEA2, and (e) the high–resolution metallic–cationic fraction in oxide films from Fig. 4.

To overcome the limitations of the high–field model and to reveal what governs the passivation process at the early times, the anodic–dissolution and film–growth models allowed us to individually study the processes kinetics of the dissolution and film formation. As shown in Fig. 6d, current decay curves of both HEAs were fitted to this model at the early time. A film–growth mechanism parameter of $n = 1$ was used to follow the two–dimensional growth and constant thickness mechanism. The corresponding fitting results are presented in Table 4, and from the fit parameters, we can calculate i_{diss}, i_{film}, and θ as a function of time, as exhibited in Fig. 7a, c.

For HEA1, the metal–anodic dissolution dominated the passivation process at the early time until $t = 20$ s, where the i_{diss} fell below i_{film}. On the contrary, the film formation and growth dominated all the passivation process for HEA2. The i_{diss} values of HEA2 were much lower, compared to those of HEA1. The fraction of the surface coverage, θ, was equal to unity ($\theta = 1$) after 30 s and 65 s for HEA1 and HEA2, respectively.

The previously calculated current density, i_{film}, was assumed to be generated during the passive film formation and thickening processes. Therefore, the charge density of $q_{film}(t)$ consumed during the process of film formation and thickening is the integral of i_{film} over time [57]:

$$q_{film}(t) = \int_{t=0}^{t} i_{film} \quad dt \tag{11}$$

As shown in Fig. 7e, the charge density increases with time for both HEAs specimens, and the $q(t)$ of HEA2 was higher than that of HEA1. Also, the charge–density variation after $\theta = 1$ for HEA1 was very small, compared to that of HEA2. The charge density for $\theta < 1$ was used during the process of forming a uniform film on the surface, and for $\theta = 1$, it was used in the process of film thickening. The passive film thickness was calculated by employing the following equation [57]:

$$h(t) = q_{film} \cdot \frac{M}{z\rho F} \tag{12}$$

where z is the charge of the cation, M is the molecular weight of the film, ρ is the density of the film, and F is Faraday's constant. Z = 3, M and ρ

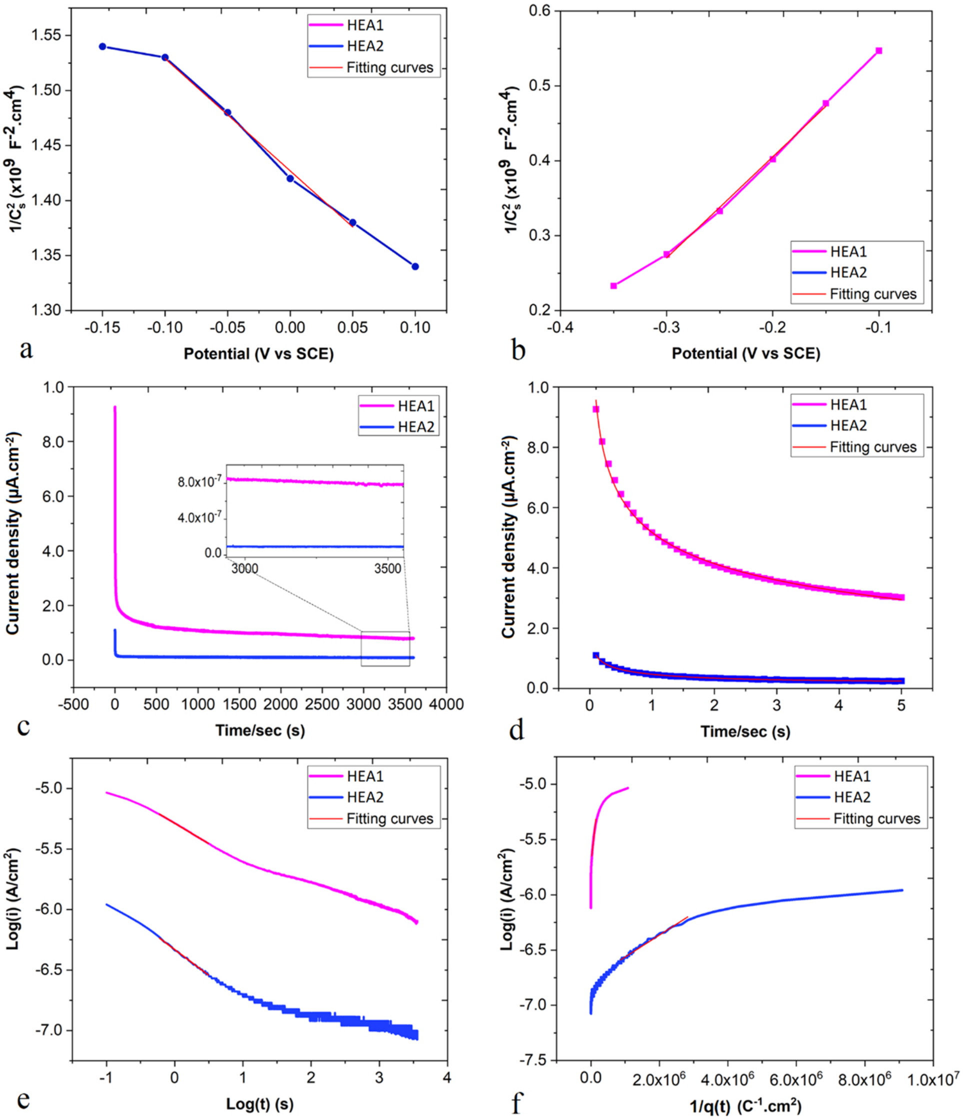

Fig. 6. (a, b) Mott–Schottky curves and potentiostatic polarization at E_{pass}: (c) current density vs. time plots, (d) the fitting of the early time stage of the current density from (c), (e) log i vs. log t plot, and (f) log i vs $1/q$ plot.

Table 4
Fitting parameters derived from Fig. 6.

Specimen	N_D or N_A ($\times 10^{21}$) /cm^3	Passivation index n	cBV (μC.cm^2)	I_{peak} ($\times 10^{-6}$ A.cm^{-2})	K (s^{-1})	A ($\times 10^{-5}$ C.cm^{-2})	b
HEA1	8.71	0.33	2.88	9.26	0.19	4.50	1.17
HEA2	5.35	0.50	0.20	1.10	0.07	2.27	1.15

are calculated from the mean values of the oxides and their fractions in Fig. 5e. From the graphical representation of the two kinetics in Fig. 7f, the thickening rate, expressed here by the slopes of the straight lines, of HEA2 was greater than that of HEA1.

4. Discussion

In comparison with Ti-6Al-4 V, as a standard stent material, HEA2 has better corrosion and pitting resistance, while HEA1 is poorer, as demonstrated by the values of E_{corr} and E_{pit} and the passivation–plateau disturbance resulting from aggressive pitting attacks. This trend can be related to the microstructural homogeneity of the single FCC–phase HEA2, unlike the microstructural heterogeneity of cuboidal $L2_1$–nanoscaled precipitates in a BCC matrix of HEA1, which generates a local electrochemical potential difference leading to selective or galvanic dissolution [58,59]. Moreover, the larger total percentage of Al and Fe concentration in HEA1 relative to that of HEA2 (70 % versus 30.26 %) may also have contributed toward the significant metal dissolution in HEA1 as both elements are quite prone to pitting corrosion under hydrochloric acid solution [60,61]. The drop in Fe content for instance can be appreciated by comparing the Fe cationic fraction extracted from the XPS in Fig. 5 (28 %) to the initial 50 % of Fe based of the nominal composition of HEA1. Furthermore, the additional presence of Ni content in HEA2 has been known to improve the resistance to pitting corrosion in general. Both factors (nano-galvanic coupling and the overall compositions) may lead to an accelerated degradation of HEA1.

The HEA2, on the other hands, has a more stable and high resistive

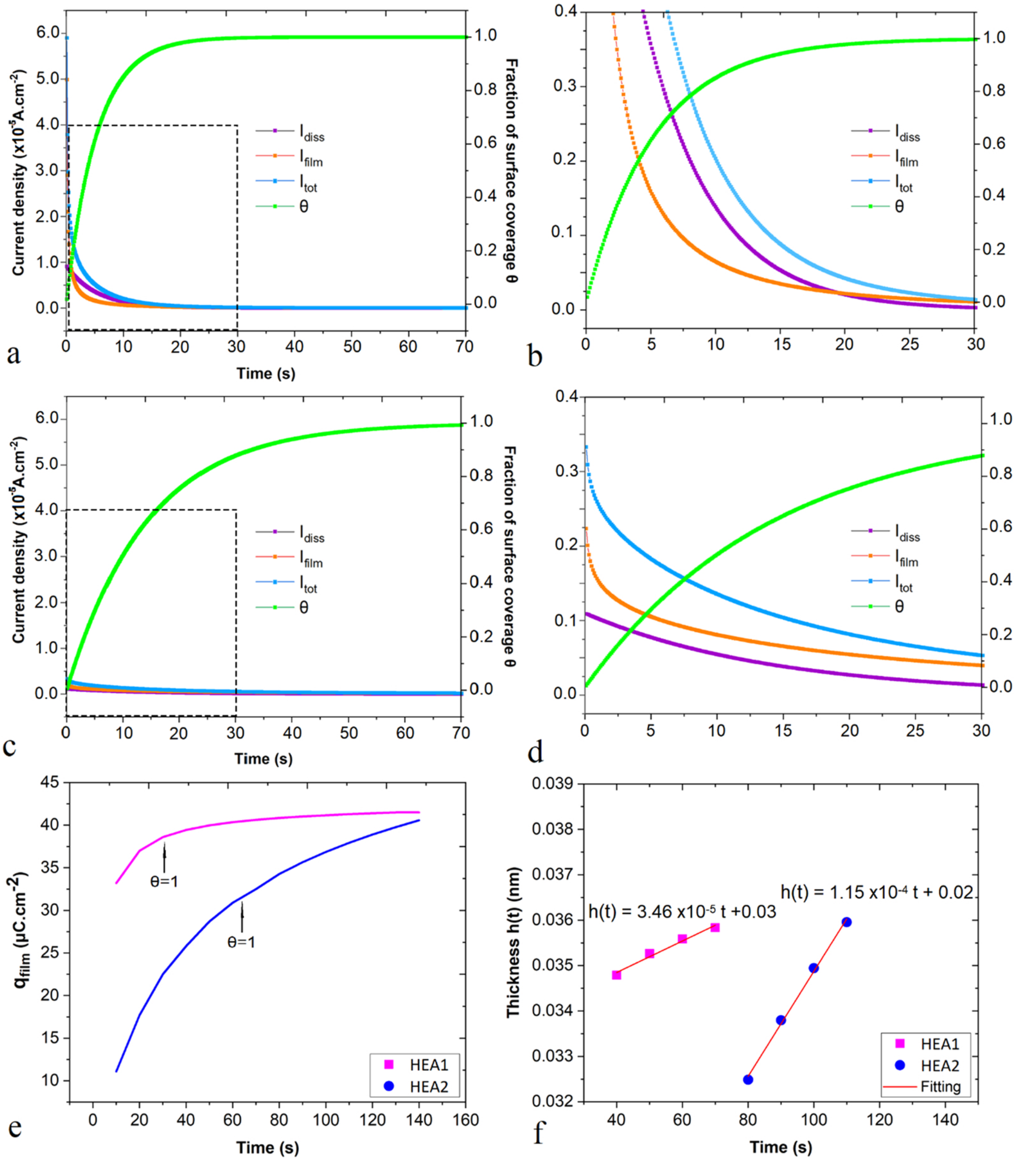

Fig. 7. Graphical representation and the zoomed parts of i_{diss}, i_{film}, and θ as a function of time according to the parameters in Table 4 for: (a, b) HEA1, (c, d) HEA2, (e) plot of q_{film} vs *time*, and (f) film thickness as a function of time.

passive film than that of HEA1, which has a low repassivation ability due to a strong electrochemical and reactional activity at the surface level [62]. As well as the lower passivation current i_{pass} measured for HEA2, which is associated to higher corrosion protection ensured by the passivation oxide. The retention of the Cr content, relative to its original nominal composition, also suggests the relatively low rate of Cr dissolution which is not necessarily common for Cr–containing alloys under Cl^- solution attack. The stable passive film of HEA2 limits the charge transfers between the metal/film and film/solution interfaces (high value of R_{ct}), with a smoother surface state (high value of n_f), similar to that of Ti-6Al-4V [63]. In the Bode diagrams, at high frequencies the value of the impedance modulus remains constant, and the phase angle is close to zero, indicating resistive–like behavior [64], while at medium and low frequencies the phase angle of HEA2 is higher, indicating better corrosion resistance [65]. On the other hand, the low values of R_{ct}, R_f and n_{dl} for HEA1 are associated with the increase in the real surface area resulting either from the active dissolution or in the pores, which leads to the increase in the surface roughness [66]. These observations are widely expected in severe localized corrosion situations.

The low value of n_{dl} can also be correlated with the selective dissolution of the precipitated phase in HEA1 [63]. The difference in the effective capacitance is due to the frequency dispersion resulting from the variation of the activity of the electrode along the surface expressing a two–dimensional or/and three–dimensional heterogeneity [67,68]. The diffusion–controlled corrosion process, as indicated by the Warburg element [69–71], can be explained by the accumulation of corrosion products in the pores, producing a concentration gradient which caused the mass transfer reaction [72]. In chlorine solutions, the formation of the chlorine complex is delayed by the diffusion of Cl^- ions from the bulk solution towards the surface of the electrode. In the pores, the presence of corrosion products limits the arrival of Cl^- ions or the diffusion of anodic products from the metal/electrolyte interface towards the bulk solution (reaction 12 – 13). There should also be the contribution of the cathodic reaction of oxygen in controlling the corrosion process. Of which a non–constant concentration of dissolved oxygen will limit the corrosion (reaction 14 – 16) [73].

$$Cl^-_{\text{(in the bulk solution)}} \rightarrow Cl^-_{\text{(adsorbed on the surface)}} \quad (13)$$

$$M^{n+}_{(metallic\ cation\ from\ the\ metal\ or\ the\ oxide)} + n\ Cl^- \rightarrow MCl_n \quad (14)$$

$$O_{2\ (\text{dissolved in the bulk solution})} \rightarrow O_{2\ (\text{dissolved at the cathodic sites})} \quad (15)$$

$$O_2 + 2H_2O + 4e^- \rightarrow 4OH^- \quad (16)$$

$$M^{n+} + n\ OH^- \rightarrow M(OH)_n \quad (17)$$

The passive film of HEA2 behaves like a p–type semiconductor due to the presence of $Cr(OH)_3$, Cr_2O_3, CoO, Co_3O_4, and $Ni(OH)_2$ [74–78], which have been linked to the high resistance of oxidation and corrosion [79–82]. In addition, the presence of the metal–OH bond at the outer side of the film reinforces and improves the resistance of the film against the species displacement and the charges transfer by reducing the number of defects and vacancies [83,84]. This trend forms a kind of amorphous structure between the inner and the outer sides of the passive film which is advantageous against cytotoxicity, of which numerous studies have demonstrated minimal interaction between blood and the amorphous oxide film [85–87], as well as many studies and reports have indicated no carcinogenic or chronic effects related to Cr(III) oxides [88, 89]. On the other hand, Cr is characterized by a free energy of formation of Cr_2O_3 and $Cr(OH)_3$ more negative than that of the oxides and hydroxides of Ni [90], therefore the presence of a high content of Cr will lead to a preferential formation of its oxides which will accelerate passivation and act as a barrier limiting the dissolution of other elements. On the contrary, the passive film of HEA1 exhibited an n–type semiconductor behavior related to the presence of Fe_2O_3, $Fe(OH)_3$, TiO_2, and MnO_2 [91–95]. The dominance of aluminum oxides affects the fraction of other passivating oxides, such as TiO_2 and Cr_2O_3, while the presence of Fe_2O_3, and especially MnO_2, reduce the quality of the passive film and its protective capacity by favoring the dissolution and the creation of defects in the passive film [52,96]. This finding is supported by the results of the Mott–Schottky analysis, where the donor density (oxygen vacancies and cation interstitials) in the n–type film of HEA1 is higher than the acceptor density (cation vacancies) in the p–type film of HEA2 [97]. The proposed film growth and dissolution mechanisms of the two specimens are illustrated in Fig. 8.

Based on the point–defect model, the passive film stabilization and pitting corrosion susceptibility are strongly associated with the semiconductor properties and the electronic structure of the film [98,99]. Oxygen vacancies and cation interstitials are generated at the metal/film interface and consumed at the film/solution interface. The accumulation of oxygen vacancies (sites of highly positive charge) attracts chloride ions and promotes their adsorption, leading to increasing the susceptibility of HEA1 to initiate pits and produce film cracking due to local tensile/fatigue stresses generated during the process of film growth [100]. The film reacts against the absorption of chloride anions by the generation of cation and/or oxygen vacancies that will attract more anions to the film/solution interface, producing an autocatalytic mechanism. The ability of the passive film to resist breakdown depends on the kinetics of the vacancies–generation and annihilation reactions. In addition, for metals with a strong affinity for complexing with chloride ions, such as iron [98], they will favor the generation of vacancies resulting from the reaction of metal–chlorides formation [101]. In the case of HEA2, the affinity of chloride ions towards p–type defects (sites of highly negative charge) is not favorable, which reduces the risk of the pitting initiation and passive film damage [98,102].

The passivation rate of HEA2 is higher than that of HEA1, as indicated by the shape of the potentiostatic polarization curves of which the transition between the two stages of kinetics process is faster for HEA2. The first stage is the rapid decrease in the current density during the first seconds under passive polarization that is mainly related to the film formation mechanism, and the second stage is the stable plateau mainly related to the film growth mechanism. This trend means that a rapid formation of protective passive film limits the electrochemical activity on the surface of HEA2, as indicated by the low steady state current density and the low starting current density pick, while HEA1 has an imperfectly stable current density plateau that continues to decrease over time.

Based on the high electric field for the ion conduction model, the rate of the passive film formation process can be indirectly expressed by the passivation index, of which the HEA2 has the highest value indicating rapid kinetics. A higher passivation index value also indicates a more compact and less defective surface quality [103,104]. The same for the *cBV* parameter that is considered as the passivation rate and passivation protection degree [50,57], which correlates with the activation energy for the transfer of charges and ions through the film. The lower *cBV* value of HEA2 means a better film protection, linked to a low activation energy or a high barrier energy limiting the conduction of ions between the two film–interfaces. The *cBV* is also associated with the measurement of the susceptibility of a passive film to stress corrosion cracking (SCC) [105]. Since SCC occurs through a repetitive process of film breakdown/dissolution/repassivation, low *cBV* (high passivation rate) leads to low SCC susceptibility, whereas high *cBV* (low passivation rate) leads to high SCC susceptibility due to a high amount of dissolution [52, 105]. By comparing the two *cBV* values for the two specimens, one may say that HEA1 has a higher susceptibility to SCC than HEA2. The *cBV* parameter is strongly related to the chemical composition of the passive film [51], and the Mn content in HEA1 increases the *cBV* value and thus increases the susceptibility to SCC [106,107]. However, an SCC experiment should be conducted to confirm this hypothesis, but beyond the scope of the present work.

Based on the anodic–dissolution and film–growth models, the different dissolution and passivation processes at an early time decay are investigated individually. The HEA2 shows a better passivation behavior and dissolution resistance and faster film growth rate than those of HEA1. This behavior is manifested by the retention of a film formation

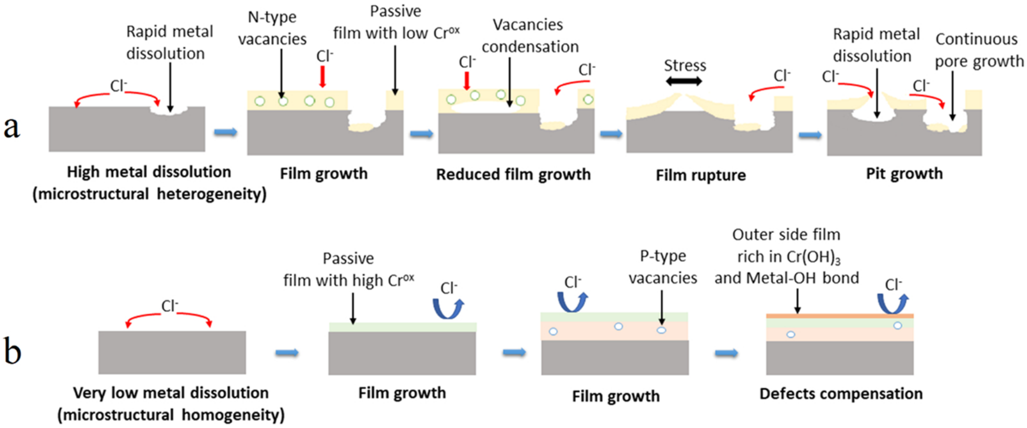

Fig. 8. Schematic illustration of film growth and dissolution mechanisms of: (a) HEA1, and (b) HEA2.

and growth current density higher than that of film dissolution throughout the passivation. On HEA1, a dominant strong dissolution activity at a very early time decay (the first 20 s) occurred until the film formation process took place. The HEA1 formed the first oxide layer more rapidly (after 30 s) than HEA2 (after 65 s), leading to a thick layer but not as compact and as stable than that of the HEA2, with high charge density values. After $\theta = 1$, the film thickening rate of HEA1 was slower than that of HEA2 due to a continuous dissolution process, which makes it prone to pitting, and stress corrosion cracking in the presence of local stresses [108].

5. Conclusion

In comparison to Ti-6Al-4 V alloy, $Al_7Cr_{23.26}Fe_{23.26}Co_{23.26}Ni_{23.26}$ (HEA2) possess better passivity and corrosion resistance in Hanks' solution at 37 °C, while $Al_{20}Cr_5Fe_{50}Mn_{20}Ti_5$ (HEA1) is poorer. The surface of both HEAs specimens was covered by a passive film composed of a mixture of Al_2O_3, Cr_2O_3, $Cr(OH)_3$, FeOOH, and Fe_2O_3 oxides. The passive film of HEA2 exhibits a p–type behavior resulting from the presence of $Cr(OH)_3$, Cr_2O_3, CoO, Co_3O_4, and $Ni(OH)_2$ known for their resistive properties, with a large fraction of Cr_2O_3 and the dominance of the metal–OH bond at the outer side of the film. This compact film exhibits a high passivation kinetics and favorable semiconductor properties, leading to a high passivation behavior and pitting resistance. The passive film of HEA1 exhibits an n–type behavior with a high concentration of defects and vacancies resulting from the presence of the Fe_2O_3, $Fe(OH)_3$, TiO_2, and MnO_2 that promotes chloride ions adsorption, leading to diffusion–controlled corrosion/dissolution and high susceptibility to pitting corrosion. The corrosion resistance of HEA1 can be further improved by promoting the presence of p–type oxides through the substitution of Al with other passivating elements of low propensity to dissolution, and reduction of Al content to lower its oxide fraction in the passive film, as well as Fe content to limit the adsorption of chloride ions. With further confirmation on its cytocompatibility, the HEA2 could become a new potential biomaterial for biomedical applications.

CRediT authorship contribution statement

A.T. Conceptualization, Methodology, Formal analysis, Writing – original draft. **R.F. and Z.L.** Formal analysis, Writing – reviewing & editing. **P.K.L.**, and **R.S.** Writing – review & editing. **H.H.** Conceptualization, Methodology, Validation, Formal analysis, Writing – reviewing & editing, Supervision, Funding acquisition. All authors have read and agreed to the published version of the manuscript.

Declaration of Competing Interest

The authors declare that they have no known competing financial interests or personal relationships that could have appeared to influence the work reported in this paper.

Data Availability

Data will be made available on request.

Acknowledgments

The present work was funded by the Natural Sciences and Engineering Research Council of Canada (NSERC) via Discovery Grant (RGPIN-2017-04274) and Alliance International Catalyst Grant, and the Canadian Foundation for Innovation (CFI) through the John R. Evans Leaders Fund (#37282). A. Tanji and H. Hermawan gratefully thank Dr. P. Chevalier of the Center for Research on Advanced Materials (CERMA) for the assistance in the XPS analysis, and Prof. Mitsuo Niinomi's team formerly at the Institute for Materials Research (IMR) Tohoku University, especially Dr. P. Fernandes Santos for providing the titanium samples. R. Feng and P. K. Liaw very much appreciate the support of the U.S. Army Research Office Project (W911NF-13-1-0438 and W911NF-19-2-0049) with the program managers, Drs. M. P. Bakas, S. N. Mathaudhu, and D. M. Stepp. Z. Lyu and P. K. Liaw thank the support from the National Science Foundation (DMR-1611180 and 1809640) with the program directors, Drs. J. Yang, G. Shiflet, and D. Farkas.

References

[1] T. Hanawa, 1 - Overview of metals and applications, in: M. Niinomi (Ed.), *Metals for Biomedical Devices, second ed.*, Woodhead Publishing, 2019, pp. 3–29.

[2] J.L. Gilbert, 1.2 Electrochemical behavior of metals in the biological milieu, in: P. Ducheyne (Ed.), *Comprehensive Biomaterials II*, Elsevier, Oxford, 2017, pp. 19–49.

[3] S. Ali, et al., Biocompatibility and corrosion resistance of metallic biomaterials, Corros. Rev. vol. 38 (5) (2020) 381–402.

[4] J.L. Gilbert, S.A. Mali, Medical implant corrosion: electrochemistry at metallic biomaterial surfaces, in: N. Eliaz (Ed.), in Degradation of Implant Materials, Springer New York, New York, NY, 2012, pp. 1–28.

[5] S. Hiromoto, 4 - Corrosion of metallic biomaterials, in: M. Niinomi (Ed.), *Metals for Biomedical Devices, second ed.*, Woodhead Publishing, 2019, pp. 131–152.

[6] D. Castro, P. Jaeger, A.C. Baptista, J.P. Oliveira, An overview of high-entropy alloys as biomaterials, Metals vol. 11 (4) (2021) 648.

[7] W. Yang, S.-J. Pang, G. Wang, Y. Liu, P.K. Liaw, T. Zhang, Ti–Zr–Hf–Nb–Ta–Sn high-entropy alloys with good properties as potential biomaterials, Rare Met. (2022) 1–11.

[8] V. Patil, S. Balivada, S. Appagana, Biomedical applications of titanium and aluminium based high entropy alloys, Int. J. Health Technol. vol. 1 (01) (2022) 40–48.

[9] B. Cantor, I. Chang, P. Knight, A. Vincent, Microstructural development in equiatomic multicomponent alloys, Mater. Sci. Eng.: A vol. 375 (2004) 213–218.

[10] D.B. Miracle, O.N. Senkov, A critical review of high entropy alloys and related concepts, Acta Mater. vol. 122 (2017) 448–511.

[11] E.P. George, D. Raabe, R.O. Ritchie, High-entropy alloys, Nat. Rev. Mater. vol. 4 (8) (2019) 515–534.

[12] Y. Zhang, et al., Microstructures and properties of high-entropy alloys, Prog. Mater. Sci. vol. 61 (2014) 1–93.

[13] Q. Pan, et al., Gradient cell–structured high-entropy alloy with exceptional strength and ductility, Science vol. 374 (6570) (2021) 984–989.

[14] W. Li, D. Xie, D. Li, Y. Zhang, Y. Gao, P.K. Liaw, Mechanical behavior of high-entropy alloys, Prog. Mater. Sci. vol. 118 (2021), 100777.

[15] Y. Shi, B. Yang, P.K. Liaw, Corrosion-resistant high-entropy alloys: a review, Metals vol. 7 (2) (2017) 43.

[16] Y. Qiu, M. Gibson, H. Fraser, N. Birbilis, Corrosion characteristics of high entropy alloys, Mater. Sci. Technol. vol. 31 (10) (2015) 1235–1243.

[17] A. Motallebzadeh, N.S. Peighambardoust, S. Sheikh, H. Murakami, S. Guo, D. Canadinc, Microstructural, mechanical and electrochemical characterization of TiZrTaHfNb and Ti1. 5ZrTa0. 5Hf0. 5Nb0. 5 refractory high-entropy alloys for biomedical applications, Intermetallics vol. 113 (2019), 106572.

[18] T. Nagase, Y. Iijima, A. Matsugaki, K. Ameyama, T. Nakano, Design and fabrication of Ti–Zr-Hf-Cr-Mo and Ti–Zr-Hf-Co-Cr-Mo high-entropy alloys as metallic biomaterials, Mater. Sci. Eng.: C. vol. 107 (2020), 110322.

[19] T. Hori, T. Nagase, M. Todai, A. Matsugaki, T. Nakano, Development of non-equiatomic Ti-Nb-Ta-Zr-Mo high-entropy alloys for metallic biomaterials, Scr. Mater. vol. 172 (2019) 83–87.

[20] M. Akmal, A. Hussain, M. Afzal, Y.I. Lee, H.J. Ryu, Systematic study of (MoTa) xNbTiZr medium-and high-entropy alloys for biomedical implants-In vivo biocompatibility examination, J. Mater. Sci. Technol. vol. 78 (2021) 183–191.

[21] W.-Y. Ching, S. San, J. Brechtl, R. Sakidja, M. Zhang, P.K. Liaw, Fundamental electronic structure and multiatomic bonding in 13 biocompatible high-entropy alloys, npj Comput. Mater. vol. 6 (1) (2020) 1–10.

[22] S. Schönecker, et al., Harnessing elastic anisotropy to achieve low-modulus refractory high-entropy alloys for biomedical applications, Mater. Des. vol. 215 (2022), 110430.

[23] X.-W. Qiu, Y.-P. Zhang, L. He, C.-g Liu, Microstructure and corrosion resistance of AlCrFeCuCo high entropy alloy, J. Alloy. Compd. vol. 549 (2013) 195–199.

[24] E.M. Godlewska, M. Mitoraj-Królikowska, J. Czerski, M. Jawańska, S. Gein, U. Hecht, Corrosion of Al (Co) CrFeNi high-entropy alloys, Front. Mater. vol. 7 (2020) 335.

[25] H. Wu, et al., Comparative study of mechanical and corrosion behaviors of cost-effective AlCrFeCoNi high entropy alloys, J. Mater. Eng. Perform. (2022) 1–11.

[26] N. Kumar, M. Fusco, M. Komarasamy, R. Mishra, M. Bourham, K. Murty, Understanding effect of 3.5 wt% NaCl on the corrosion of Al0. 1CoCrFeNi high-entropy alloy, J. Nucl. Mater. vol. 495 (2017) 154–163.

[27] D. Kumar, O. Maulik, V. Sharma, Y. Prasad, V. Kumar, Understanding the effect of tungsten on corrosion behavior of AlCuCrFeMnWx high-entropy alloys in 3.5 wt % NaCl solution, J. Mater. Eng. Perform. vol. 27 (9) (2018) 4481–4488.

[28] Y. Shi, B. Yang, X. Xie, J. Brechtl, K.A. Dahmen, P.K. Liaw, Corrosion of Al xCoCrFeNi high-entropy alloys: Al-content and potential scan-rate dependent pitting behavior, Corros. Sci. vol. 119 (2017) 33–45.

[29] R. Wang, K. Zhang, C. Davies, X. Wu, Evolution of microstructure, mechanical and corrosion properties of AlCoCrFeNi high-entropy alloy prepared by direct laser fabrication, J. Alloy. Compd. vol. 694 (2017) 971–981.

[30] K. Kuwabara, H. Shiratori, T. Fujieda, K. Yamanaka, Y. Koizumi, A. Chiba, Mechanical and corrosion properties of AlCoCrFeNi high-entropy alloy fabricated with selective electron beam melting, Addit. Manuf. vol. 23 (2018) 264–271.

[31] L. Zhang, J. Xu, J. Chen, J. Huang, J. Luo, Microstructure and corrosion resistance of AlCoCrFeNi high-entropy alloy coating on sintered NdFeB magnets prepared by HVOF spraying, J. Magn. Magn. Mater. vol. 551 (2022), 169136.

[32] A. Meghwal, et al., Multiscale mechanical performance and corrosion behaviour of plasma sprayed AlCoCrFeNi high-entropy alloy coatings, J. Alloy. Compd. vol. 854 (2021), 157140.

[33] R. Feng, et al., Phase stability and transformation in a light-weight high-entropy alloy, Acta Mater. vol. 146 (2018) 280–293.

[34] C. f. D. R. Health, Biological Responses to Metal Implants, US Food and Drug Administration, 2019.

[35] A. International, R.J. Narayan, Materials for Medical Devices, ASM International, 2012.

[36] H. Diao, et al., Novel NiAl-strengthened high entropy alloys with balanced tensile strength and ductility, Mater. Sci. Eng.: A vol. 742 (2019) 636–647.

[37] R. Feng, et al., High-throughput design of high-performance lightweight high-entropy alloys, Nat. Commun. vol. 12 (1) (2021) 1–10.

[38] B. Hirschorn, M.E. Orazem, B. Tribollet, V. Vivier, I. Frateur, M. Musiani, Constant-phase-element behavior caused by resistivity distributions in films: I. Theory, J. Electrochem. Soc. vol. 157 (12) (2010) C452.

[39] M.E. Orazem, et al., Dielectric properties of materials showing constant-phase-element (CPE) impedance response, J. Electrochem. Soc. vol. 160 (6) (2013) C215.

[40] P. Córdoba-Torres, T.J. Mesquita, R.P. Nogueira, Relationship between the origin of constant-phase element behavior in electrochemical impedance spectroscopy and electrode surface structure, J. Phys. Chem. C vol. 119 (8) (2015) 4136–4147.

[41] S. Marcelin, Z. Zhang, B. Ter-Ovanessian, B. Normand, Relationship between the resistivity profiles obtained from the power law model and the physico-chemical properties of passive films, J. Electrochem. Soc. vol. 168 (2) (2021), 021503.

[42] G. Brug, A.L. van den Eeden, M. Sluyters-Rehbach, J.H. Sluyters, The analysis of electrode impedances complicated by the presence of a constant phase element, J. Electroanal. Chem. Interfacial Electrochem. vol. 176 (1–2) (1984) 275–295.

[43] X. Cheng, X. Li, C. Du, Properties of passive film formed on 316L/2205 stainless steel by Mott-Schottky theory and constant current polarization method, Chin. Sci. Bull. vol. 54 (13) (2009) 2239–2246.

[44] J. Robertson, High dielectric constant oxides, Eur. Phys. J. -Appl. Phys. vol. 28 (3) (2004) 265–291.

[45] S.S. Djokić, Biomedical Applications. Business Media, Springer Science, 2012.

[46] R.A. Lunt, A.J. Jackson, A. Walsh, Dielectric response of Fe2O3 crystals and thin films, Chem. Phys. Lett. vol. 586 (2013) 67–69.

[47] P. Engseth, J. Scully, Repassivation studies on an austenitic stainless steel in chloride solutions, Corros. Sci. vol. 15 (6–12) (1975) 505–519.

[48] G. Burstein, P. Marshall, Growth of passivating films on scratched 304L stainless steel in alkaline solution, Corros. Sci. vol. 23 (2) (1983) 125–137.

[49] J.-B. Lee, Effects of alloying elements, Cr, Mo and N on repassivation characteristics of stainless steels using the abrading electrode technique, Mater. Chem. Phys. vol. 99 (2–3) (2006) 224–234.

[50] R.M. Fernández-Domene, E. Blasco-Tamarit, D.M. García-García, J. García-Antón, Cavitation corrosion and repassivation kinetics of titanium in a heavy brine LiBr solution evaluated by using electrochemical techniques and Confocal Laser Scanning Microscopy, Electrochim. Acta vol. 58 (2011) 264–275.

[51] E.-A. Cho, C.-K. Kim, J.-S. Kim, H.-S. Kwon, Quantitative analysis of repassivation kinetics of ferritic stainless steels based on the high field ion conduction model, Electrochim. Acta vol. 45 (12) (2000) 1933–1942.

[52] I. Toor, Repassivation kinetics and its role in SCC prediction-a review, Int. J. Electrochem. Sci. vol. 9 (2014) 2737–2755.

[53] Z. Que, T. Saario, A. Toivonen, U. Ehrnstén, Stress corrosion cracking initiation susceptibility of Alloy 182 with different surface treatments, Corros. Sci. vol. 196 (2022), 110037.

[54] L.R. Goodman, P.M. Singh, Repassivation behavior of X65 pipeline steel in fuel grade ethanol and its implications for the stress corrosion cracking mechanism, Corros. Sci. vol. 65 (2012) 238–248.

[55] R. Lillard, G. Vasquez, D. Bahr, The kinetics of anodic dissolution and repassivation on stainless steel 304L in solutions containing nitrate, J. Electrochem. Soc. vol. 158 (6) (2011) C194.

[56] R. Nakamura, D. Tokozakura, H. Nakajima, J.-G. Lee, H. Mori, Hollow oxide formation by oxidation of Al and Cu nanoparticles, J. Appl. Phys. vol. 101 (7) (2007), 074303.

[57] H. Xu, D. Sun, H. Yu, Repassivation behavior of 316L stainless steel in borate buffer solution: Kinetics analysis of anodic dissolution and film formation, Appl. Surf. Sci. vol. 357 (2015) 204–213.

[58] A.V. Ayyagari, B. Gwalani, S. Muskeri, S. Mukherjee, R. Banerjee, Surface degradation mechanisms in precipitation-hardened high-entropy alloys, NPJ Mater. Degrad. vol. 2 (1) (2018) 1–10.

[59] L. Du, et al., Inhomogeneous phases in Cu-Zn-Al-Fe-Mn and the micro-galvanic coupling in 3.5 wt% NaCl solutions at different pH, Corros. Sci. vol. 195 (2022), 110005.

[60] A.A. El-Awady, B.A. Abd-El-Nabey, S.G. Aziz, Thermodynamic and kinetic factors in chloride ion pitting and nitrogen donor ligand inhibition of aluminium metal corrosion in aggressive acid media, J. Chem. Soc. Faraday Trans. vol. 89 (5) (1993) 795–802, https://doi.org/10.1039/FT9938900795.

[61] G.S. Frankel, Pitting corrosion of metals: a review of the critical factors, 1998/06/01, J. Electrochem. Soc. vol. 145 (6) (1998) 2186–2198, https://doi.org/10.1149/1.1838615.

[62] S. Esmailzadeh, M. Aliofkhazraei, H. Sarlak, Interpretation of cyclic potentiodynamic polarization test results for study of corrosion behavior of metals: a review, Prot. Met. Phys. Chem. Surf. vol. 54 (5) (2018) 976–989.

[63] K. Yamanaka, et al., Corrosion mechanism of an equimolar AlCoCrFeNi high-entropy alloy additively manufactured by electron beam melting, npj Mater. Degrad. vol. 4 (1) (2020) 1–12.

[64] S. Fajardo, D.M. Bastidas, M. Criado, J. Bastidas, Electrochemical study on the corrosion behaviour of a new low-nickel stainless steel in carbonated alkaline solution in the presence of chlorides, Electrochim. Acta vol. 129 (2014) 160–170.

[65] H. Luo, Z. Li, A.M. Mingers, D. Raabe, Corrosion behavior of an equiatomic CoCrFeMnNi high-entropy alloy compared with 304 stainless steel in sulfuric acid solution, Corros. Sci. vol. 134 (2018) 131–139.

[66] N. Mahato, M. Singh, Investigation of passive film properties and pitting resistance of AISI 316 in aqueous ethanoic acid containing chloride ions using electrochemical impedance spectroscopy (EIS), Port. Electrochim. Acta vol. 29 (4) (2011) 233–251.

[67] B. Hirschorn, M.E. Orazem, B. Tribollet, V. Vivier, I. Frateur, M. Musiani, Determination of effective capacitance and film thickness from constant-phase-element parameters, Electrochim. Acta vol. 55 (21) (2010) 6218–6227.

[68] B. Tribollet, Analysis of constant phase element, Electrochem. Soc. (2013).

[69] D. Sun, et al., Pitting corrosion behavior of stainless steel in ultrasonic cell, Electrochim. Acta vol. 54 (5) (2009) 1558–1563.

[70] E.P. Randviir, C.E. Banks, Electrochemical impedance spectroscopy: an overview of bioanalytical applications, Anal. Methods vol. 5 (5) (2013) 1098–1115.

[71] A. Yavuz, Copper-and nickel-based flexible polyester electrodes for energy storage devices, J. Mater. Res. vol. 35 (16) (2020) 2115–2125.

[72] S. Ahn, Y. Choi, J. Kim, J. Han, A study on corrosion resistance characteristics of PVD Cr-N coated steels by electrochemical method, Surf. Coat. Technol. vol. 150 (2–3) (2002) 319–326.

[73] M.C. Quevedo, G. Galicia, R. Mayen-Mondragon, J.G. Llongueras, Role of turbulent flow seawater in the corrosion enhancement of an Al–Zn–Mg alloy: an electrochemical impedance spectroscopy (EIS) analysis of oxygen reduction reaction (ORR), J. Mater. Res. Technol. vol. 7 (2) (2018) 149–157.

[74] Q. Zhang, Y. Xu, X. Wang, The electrochemical behavior of Ni (OH) 2 in KOH solution containing aluminum hydroxide, Mater. Chem. Phys. vol. 86 (2–3) (2004) 293–297.

[75] M. Pontinha, S. Faty, M. Walls, M. Ferreira, M.D.C. Belo, Electronic structure of anodic oxide films formed on cobalt by cyclic voltammetry, Corros. Sci. vol. 48 (10) (2006) 2971–2986.

[76] M. Cosio, M. Scampicchio, S. Benedetti, Electronic Noses and Tongues, Academic Press, Boston, MA, USA, 2012.

[77] K. Morshed-Behbahani, P. Najafisayar, M. Pakshir, M. Shahsavari, An electrochemical study on the effect of stabilization and sensitization heat treatments on the intergranular corrosion behaviour of AISI 321H austenitic stainless steel, Corros. Sci. vol. 138 (2018) 28–41.

[78] Y. Zhang, H. Luo, Q. Zhong, H. Yu, J. Lv, Characterization of passive films formed on as-received and sensitized AISI 304 stainless steel, Chin. J. Mech. Eng. vol. 32 (1) (2019) 1–12.

[79] K.H. Kim, S.H. Lee, N.D. Nam, J.G. Kim, Effect of cobalt on the corrosion resistance of low alloy steel in sulfuric acid solution, Corros. Sci. vol. 53 (11) (2011) 3576–3587.

[80] R. Galo, R.F. Ribeiro, R.C.S. Rodrigues, L.A. Rocha, M. d G.C. d Mattos, Effects of chemical composition on the corrosion of dental alloys, Braz. Dent. J. vol. 23 (2) (2012) 141–148.

[81] L. Xu, B. Wang, J. Zhu, W. Li, Z. Zheng, Effect of Cr content on the corrosion performance of low-Cr alloy steel in a CO_2 environment, Appl. Surf. Sci. vol. 379 (2016) 39–46.

[82] C.-C. Yen, et al., Corrosion mechanism of annealed equiatomic AlCoCrFeNi tri-phase high-entropy alloy in 0.5 M H2SO4 aerated aqueous solution, Corros. Sci. vol. 157 (2019) 462–471.

[83] M. Ben-Haim, U. Atzmony, N. Shamir, Studies of metal-oxygen bonds on 18%-Cr stainless steel in the passive and transpassive regions by integrated and angle-resolved X-ray photoelectron spectroscopies, Corrosion vol. 44 (7) (1988) 461–464.

[84] J. Bhattarai, Angle resolver X-ray photoelectron spectroscopic analysis of the passive film of the corrosion-resistant W-32Zr alloy in 12 M HCl solution, Bangladesh J. Sci. Ind. Res. vol. 49 (2) (2014) 103–110.

[85] C.C. Shih, S.J. Lin, K.H. Chung, Y.L. Chen, Y.Y. Su, Increased corrosion resistance of stent materials by converting current surface film of polycrystalline oxide into amorphous oxide, J. Biomed. Mater. Res.: Off. J. Soc. Biomater. Jpn. Soc. Biomater. Aust. Soc. Biomater. Korean Soc. Biomater. vol. 52 (2) (2000) 323–332.

[86] C.C. Shih, C.M. Shih, Y.Y. Su, S.J. Lin, Antithrombogenic oxide film on stainless steel for cardiovascular applications, Wire J. Int. vol. 37 (10) (2004) 64–69.

[87] C. Shih, C. Shih, Y. Su, S. Lin, Amorphous oxide film on stainless steel for cardiovascular applications *Trans. -7th World Biomater. Congr.* 2004 530.

[88] E.C. Compounds Hazard Summary Natl. Cent. Environ. Assess. (NCEA): Wash., DC, USA 1973 639 700.

[89] N.J.D. o H. a S. Services Hazardous substance fact sheet for Chromic oxides N. Jersey Dep. Health Sr. Serv. 2005.

[90] L.E. Eiselstein, D. Proctor, T. Flowers, Trivalent and hexavalent chromium issues in medical implants, in: *Materials Science Forum*, vol. 539, Trans Tech Publ, 2007, pp. 698–703.

[91] J.O.M. Bockris, Y. Kang, The protectivity of aluminum and its alloys with transition metals, J. Solid State Electrochem. vol. 1 (1) (1997) 17–35.

[92] L. Guo, S. Qin, B. Yang, D. Liang, L. Qiao, Effect of hydrogen on semiconductive properties of passive film on ferrite and austenite phases in a duplex stainless steel, Sci. Rep. vol. 7 (1) (2017) 1–6.

[93] S. Kobayashi, M. Ichimura, Electrochemical deposition of Cu-doped p-type iron oxide thin films, Semicond. Sci. Technol. vol. 33 (10) (2018), 105006.

[94] J. Lu, W. Zhang, W. Huo, Y. Zhao, W. Cui, Y. Zhang, Electrochemical corrosion behavior and mechanical properties of nanocrystalline Ti–6Al–4V alloy induced by sliding friction treatment, Materials vol. 12 (5) (2019) 760.

[95] S.K. Ghosh, Diversity in the family of manganese oxides at the nanoscale: from fundamentals to applications, ACS Omega vol. 5 (40) (2020) 25493–25504.

[96] A. Tanji, F. Gapsari, A. Syahrom, M.H. Idris, H. Hermawan, Effect of Mo addition on the pitting resistance of TiMn alloys in Hanks' solution, J. Alloy. Compd. vol. 871 (2021), 159582.

[97] Y. Zhang, D.D. Macdonald, M. Urquidi-Macdonald, G.R. Engelhardt, R.B. Dooley, Passivity breakdown on AISI Type 403 stainless steel in chloride-containing borate buffer solution, Corros. Sci. vol. 48 (11) (2006) 3812–3823.

[98] D.D. Macdonald, The point defect model for the passive state, J. Electrochem. Soc. vol. 139 (12) (1992) 3434.

[99] D.D. Macdonald, The history of the point defect model for the passive state: a brief review of film growth aspects, Electrochim. Acta vol. 56 (4) (2011) 1761–1772.

[100] Z. Qin, X. Pang, Y. Yan, L. Qiao, H.T. Tran, A.A. Volinsky, Passive film-induced stress and mechanical properties of α-Ti in methanol solution, Corros. Sci. vol. 78 (2014) 287–292.

[101] J. Amri, T. Souier, B. Malki, B. Baroux, Effect of the final annealing of cold rolled stainless steels sheets on the electronic properties and pit nucleation resistance of passive films, Corros. Sci. vol. 50 (2) (2008) 431–435.

[102] C.B. Nascimento, U. Donatus, C.T. Rios, R.A. Antunes, Electronic properties of the passive films formed on CoCrFeNi and CoCrFeNiAl high entropy alloys in sodium chloride solution, J. Mater. Res. Technol. vol. 9 (6) (2020) 13879–13892.

[103] Z. Szklarska-Smialowska, Pitting corrosion of aluminum, Corros. Sci. vol. 41 (9) (1999) 1743–1767.

[104] C. Pan, L. Liu, Y. Li, B. Zhang, F. Wang, The electrochemical corrosion behavior of nanocrystalline 304 stainless steel prepared by magnetron sputtering, J. Electrochem. Soc. vol. 159 (11) (2012) C453.

[105] H.-S. Kwon, E. Cho, K. Yeom, Prediction of stress corrosion cracking susceptibility of stainless steels based on repassivation kinetics, Corrosion vol. 56 (1) (2000) 32–40.

[106] K.J. Park, H. Kwon, Manganese effects on repassivation kinetics and SCC susceptibility of high Mn–N austenitic stainless steel alloys, J. Electrochem. Soc. vol. 154 (9) (2007) C494.

[107] K. Park, H. Kwon, Effects of Mn on the localized corrosion behavior of Fe–18Cr alloys, Electrochim. Acta vol. 55 (9) (2010) 3421–3427.

[108] Z. Wu, et al., Thickness-dependent pitting corrosion behavior in Ni–Nb thin film metallic glass, Thin Solid Films vol. 564 (2014) 294–298.